# Single-nucleus transcriptomic mapping uncovers targets for traumatic brain injury

Qiuyun Yang, Lingxuan Zhang, Manrui Li, et al.

*Genome Res.* published online September 20, 2023
Access the most recent version at doi:10.1101/gr.277881.123

# Single-nucleus transcriptomic mapping uncovers targets for traumatic brain injury

Qiuyun Yang[1,2,†], Lingxuan Zhang[3,†], Manrui Li[1,†], Yang Xu[1], Xiaogang Chen[4], Ruixuan Yuan[3], Xiaofeng Ou[5], Min He[5], Miao Liao[1], Lin Zhang[6], Hao Dai[4], Meili Lv[7], Xiaoqi Xie[5,*], Weibo Liang[1,*], Xiameng Chen[4,*]

1. Department of Forensic Genetics, West China School of Basic Medical Sciences and Forensic Medicine, Sichuan University, Chengdu 610000, China
2. West China Second University Hospital, Sichuan University, Chengdu 610041, China.
3. West China School of Basic Medical Sciences and Forensic Medicine, Sichuan University, Chengdu 610000, China
4. Department of Forensic Pathology and Forensic Clinical Medicine, West China School of Basic Medical Sciences and Forensic Medicine, Sichuan University, Chengdu 610000, China
5. Department of Critical Care Medicine, Sichuan University, Chengdu 610000, China
6. Sichuan University, Chengdu 610041, China
7. Department of Immunology, West China School of Basic Medical Sciences and Forensic Medicine, Sichuan University, Chengdu 610000, China

†These authors contributed equally to this work.

[*]**Corresponding authors:**

**Xiameng Chen** Associate Professor, Department of Forensic Pathology and Forensic Clinical Medicine, West China School of Basic Medical Sciences and Forensic Medicine, Sichuan University, Chengdu, China. Email: xmchen990@gmail.com.

**Weibo Liang** Professor, Vice President, Department of Forensic Genetics, West China School of Basic Medical Sciences and Forensic Medicine, Sichuan University, Chengdu, China. Email: liangweibo@gmail.com.

**Xiaoqi Xie** Professor, Vice director, Department of Critical Care Medicine, Sichuan University, Chengdu, China. Email: xiaoqixie1898060@163.com.

## Abstract

The subventricular zone (SVZ) is a neurogenic niche that contributes to homeostasis and repair after brain injury. However, the effects of mild traumatic brain injury (mTBI) on the divergence of the regulatory DNA landscape within the SVZ and its link to functional alterations remain unexplored. In this study, we meticulously mapped the transcriptome atlas of murine SVZ and its responses to mTBI at the single-cell level. We observed cell-specific gene expression changes following mTBI and unveiled diverse cell-to-cell interaction networks that influence a wide array of cellular processes. Moreover, we reported novel neurogenesis lineage trajectories and related key transcription factors, which we subsequently validated through loss-of-function experiments. Specifically, we validated the role of *Tcf7l1*, a cell cycle gene regulator, in promoting neural stem cell differentiation towards the neuronal lineage after mTBI, providing a potential target for regenerative medicine. Overall, our study profiles an SVZ transcriptome reference map, which underlies the differential cellular behavior in response to mTBI. The identified key genes and pathways that may ameliorate brain damage or facilitate neural repair serve as valuable resources for drug discovery in the context of mTBI.



## Key Words

traumatic brain injury, single nucleus sequencing, neural stem cell, differentiation, neurogenesis

## Introduction

Mild traumatic brain injury (mTBI) is the most common type of traumatic brain injury (Silverberg et al. 2020). A single mTBI can trigger pathophysiological changes in the brain, resulting in acute neurological dysfunction and a range of subsequent post-acute or chronic sequelae (Mychasiuk et al. 2014; Collins-Praino et al. 2018). Nevertheless, specific and effective mTBI biomarkers are currently lacking, and the clinical outcomes of patients with mTBI are unsatisfactory.

The subventricular zone (SVZ) is a neurogenic niche in the adult brain responsible for maintaining tissue homeostasis and recovery after brain stimulation (Chavali et al. 2018). This neurogenic niche is an intricate microenvironment comprising morphologically and molecularly distinct subtypes of neural stem cells (NSCs) that give rise to specific progenitor cell types committed to either neuronal or glial differentiation (Doetsch et al. 1999; Buono et al. 2012). Upon brain injury, NSCs in the SVZ undergo reprogramming to induce neurogenesis (Llorens-Bobadilla et al. 2015). Although progress has been made in characterizing NSC proliferation and differentiation during neurogenesis, their diversity, responsive heterogeneity, and governing factors are not entirely clear. In addition, the number of newly generated neurons is insufficient to fully compensate for the loss of neurons caused by the injury (Cao et al. 2002). Therefore, it is essential to comprehend the diversity and potential of niche cells, their dynamics upon injury, and the

77 underlying principles of their regulation to elucidate mTBI pathogenesis and
78 identify relevant diagnostic or therapeutic targets.

79 While recent advancements in snRNA-seq have contributed to unraveling the
80 heterogeneity of the SVZ under physiological circumstances (Zywitza et al.
81 2018; Xie et al. 2020), the impact of mTBI on SVZ remains unexplored,
82 leaving a critical void in understanding of the post-injury dynamics within this
83 region. The primary purpose of our study is to use droplet-based snRNA-seq
84 to examine cellular and molecular heterogeneity within the SVZ niche under
85 both normal and mTBI conditions. The data obtained from this study will
86 serve as a crucial resource for investigating adult neurogenesis and its
87 governing mechanisms. Additionally, we aim to leverage this data resource to
88 explore and validate novel targets that have the potential to enhance
89 neurogenesis after mTBI.

90 **Results**

91 *Single-Cell Profiling of the Entire Adult SVZ Niche*

92 In this study, we investigated how the adult SVZ changes at the single-cell
93 level under mTBI (Fig. 1A). The Neurological Severity Score (NSS) (Fig. 1B)
94 revealed a significant difference between the CCI and sham-operated group 1
95 h post-injury. The NSS results, consistent with previous mTBI studies,
96 indicated mild brain impairment (Huynh et al. 2020) (Fig. 1B). To elucidate
97 the specific gene expression features of each cell type in the SVZ niche under

CCI insult, we profiled single-nucleus sequencing of matched SVZs from three mTBI mice and three sham-operated controls (Fig. 1C). Specifically, the lateral ventricular wall of each mouse was micro-dissected and digested into individual cells, which were then suspended using an optimized protocol without cell sorting to best preserve *in vivo* conditions (Biancalani et al. 2021). We utilized a chromium controller chip to load the pooled samples, barcode each cell, prepare an mRNA library, and perform sequencing. Following quality control filtering, 15,265 single cells with an average of 6,948 detected unique molecular identifiers and an average of 2,542 genes in each cell were retained for subsequent analysis (Supplemental Fig S1A).

Sequencing data were normalized using SCTransform. Subsequent data dimension reduction and visualization were achieved via PCA and UMAP using the Seurat algorithm (Stuart et al. 2019) (https://satijalab.org/seurat/) (Fig. 1A and Supplemental Fig S1B). The 17 designated clusters were classified into 7 major cell types using previously known markers (Luo et al. 2015; Shah et al. 2018; Zywitza et al. 2018; Mizrak et al. 2019) (Supplemental Table S1). Considering that SVZ astrocytes share many hallmarks with NSCs and are generally believed to function as NSCs in this neurogenic niche (Llorens-Bobadilla et al. 2015), we grouped clusters 4, 5, and 10 together as "NSCs & astrocytes." (Fig. 1D-E, Supplemental Fig S1C, and Supplemental Table S2). GO analysis of differentially expressed genes (DEGs) across cell types revealed biological processes consistent with previously known functions (Fig. 1E). For

instance, the terms “dendrite development” in neurons, “myelination” in oligodendrocytes, and “neural precursor cell proliferation” in NSCs & astrocytes. These results further support our classification of the cell clusters.

Based on cell clustering and classification, we identified genes exclusively expressed in individual cell types, which were previously unknown. These cell type-specific genes included *Prr5l* in oligodendrocytes, *Kank1* in oligodendrocyte precursor cell (OPC), *Rorb* in NSCs & astrocytes, *Fgfbr2* in microglia, *Mecom* in endothelial and mural cells, and *Dnah12* in ependymal cells (Supplemental Fig S2A), which could potentially serve as novel markers for each cell type. We utilized the SVZ single-cell dataset from previous studies to validate these markers and confirm their accuracy (Supplemental Fig S2B-C) (Zywitza et al. 2018; Batiuk et al. 2020). Collectively, this profile represents the first single-nucleus transcriptome map of rodent SVZ under mTBI.

*Each SVZ Cell Type Showed Transcriptome Alterations in Response to mTBI*

To elucidate the molecular mechanisms underlying mTBI pathogenesis, we compared the cellular and transcriptional differences between the mTBI and control groups (Fig. 2A-B). First, we examined the proportion of each cluster in both groups and validated the results using scCODA (Buttner et al. 2021) (Supplemental Table S3). Compared to the control group, scCODA suggested the proportion of neurons in the mTBI group largely decreased, while OPCs,

oligodendrocytes, and microglia were more abundant (Fig. 2A). These shifts are consistent with reports of neuronal loss (Bu et al. 2016; Holden et al. 2021; Jamjoom et al. 2021) and glial responses post-injury, such as neuroinflammatory responses induced by microglia and demyelination related to oligodendrocyte pathology (Chiu et al. 2016; Furtado et al. 2021; Matson et al. 2022). Notably, clusters 13 and 15, two neuron subtypes, were only observed in the mTBI group (Fig. 2B). Cluster 13 highly expressed the genes *Shox2*, *Slc17a6* and *Grid2ip* (Supplemental Fig S3A and Supplemental Table S1), most of which were synapse-related (Supplemental Fig S3A) (Dougherty et al. 2013; Matson et al. 2022). The enriched genes in cluster 15 mainly participated in various metabolic and biosynthetic processes (Supplemental Fig S3B), which suggested a metabolically active state. However, whether these novel mTBI-induced subtypes are newly generated neurons or previously uncharacterized neuronal states/identities still needs further validation.

The mTBI-associated transcriptional changes in individual cell types were investigated based on the regional gene set defined above (Fig. 2C-D and Supplemental Table S4). Identified DEGs were evaluated and annotated using GO and the Kyoto Encyclopedia of Genes and Genomes, which helped explain the fundamental mechanisms of mTBI pathogenesis (Fig. 2C-D and Supplemental Fig S3C). Diverse biological processes were activated after mTBI, including “learning” in neurons, “post-synapse organization” in

oligodendrocytes, and “autophagy” and “receptor-mediated endocytosis” in microglia. In addition, we plotted certain signaling pathways using UMAP, achieving an intuitive visualization of cell-specific enrichment and alterations (Fig. 2E). For instance, “long-term potential” was down-regulated in neurons post-injury, “nucleotide excision repair” was activated in certain NSC & astrocyte subtypes, while the “PPAR signaling pathway” was augmented in other subtypes. Altogether, this cell type-specific transcriptome atlas elucidates the cellular basis of mTBI pathogenesis, providing a resource for future investigations into SVZ pathophysiological processes at the cell-type resolution.

*mTBI Induced Extensive Reorganization of Cell-Cell Interactions in the SVZ*

Cellular function and behavior can also be influenced by cell-cell interactions. Therefore, we conducted a survey of the expression of various ligand-receptor pairs to predict cellular crosstalk in the SVZ using CellChat (Jin et al. 2021; Zhao et al. 2022) (Supplemental Fig S4A). To explore ligand-receptor interaction patterns, cell types and pathways were clustered according to the similarity of incoming or outgoing signaling (Supplemental Fig S4A). For instance, the incoming communication of the targeted cells encompasses four different patterns. Microglia incoming communication comprises a pattern that includes the epigenetic regulator GAS, colony-stimulating factor (CSF), chemokines, such as CX3C, and TGF-β (Supplemental Fig S4A). OPCs and NSCs & astrocytes were assigned to another pattern, involving growth factors,

185 such as PDGF, EGF, and the neurogenesis-associated factor NRG.

186 By calculating the numbers and weights of these ligand-receptor pairs (Fig.
187 3A-C), we found that the total number of inferred interactions increased, and
188 interaction strength was enhanced in response to mTBI (Fig. 3B). The most
189 flexible cell types were oligodendrocytes, NSCs & astrocytes, and neurons (Fig.
190 3C). Notably, the communication between neurons and NSCs & astrocytes was
191 relatively more enhanced among all cell types after mTBI (Fig. 3A), consistent
192 with the reports of significant astrocyte-neuron crosstalk under adverse
193 stimulation (Volterra and Meldolesi 2005; Barreto et al. 2011). However,
194 communication between neurons and NSCs has not been studied. Here, we
195 found that these two cell types interact via the *Tgfa-Efgr* and *Erg1/2/3-Erbb4*
196 pairs. These ligand receptors are known to participate in progenitor cell
197 proliferation (Seshadri et al. 2010), indicating that insulted neurons may
198 release signals to NSCs following mTBI to promote neurogenesis via these
199 pairs. Additionally, we characterized the major pathways of the affected
200 ligand-receptor pairs (Fig. 3D-E) to visualize the detailed reorganization of
201 cell-to-cell signaling. For instance, CSF signaling, a pathway known to induce
202 inflammatory responses and microglia proliferation after brain injury (Wyss-
203 Coray 2006; Luo et al. 2013), was significantly enhanced between microglia
204 and endothelial cells in the mTBI SVZ (Fig. 3D). Whether endothelia play a
205 role in microglial behavior post-injury remains to be elucidated (Fig. 3A).
206 Taken together, the breadth of our study enables us to disclose elaborate

alterations in the molecular network after mTBI, pinpointing potential targets for its treatment or diagnosis.

### *Niche NSCs & Astrocytes Exhibited Strong Heterogeneity within the Neurogenic Lineage*

To comprehensively characterize NSC heterogeneity within the SVZ, we conducted further resolution of the original "NSCs & astrocytes" cell type (Fig. 4A and Supplemental Table S5) into 5 subtypes based on unbiased clustering and previously known markers (Llorens-Bobadilla et al. 2015; Shah et al. 2018). By comparison, we identified several potential novel markers specific to individual subtypes (Fig. 4B). For instance, *Mertk* and *Grin2c* were especially enriched in niche astrocytes, but barely expressed in quiescent NSC (qNSC) (Fig. 4B); thus, they can be potentially employed as markers to distinguish these two cell types, which has long been a challenge. Other markers, such as *Kank1* and *Ntsr2* for qNSC (Shah et al. 2018; Kim et al. 2022), *Adamts18* and *Thbs4* for early actively dividing NSCs (aNSCs) (Beckervordersandforth et al. 2010), *Egfr* and *Mms22l* for late aNSCs (Pluchino and Nicaise 2021), and *Cpne4* and *Dcx* for neuroblasts (Kim et al. 2022) (Fig. 4B), also exhibited specific expression and deserve future downstream validation.

Based on the above sub-clustering, we found that the proportion of late aNSCs and qNSCs increased in the acute post-injury stage, while the proportion of

early aNSCs, astrocytes, and neuroblasts decreased (Fig. 4C), the significant change of qNSCs has also been validated using scCODA (Buttner et al. 2021) (Supplemental Table S3). This shift indicated that mTBI may promote SVZ cell differentiation from early to late aNSCs and their descendants to counterbalance cell loss caused by the sustained damage. Nevertheless, the descendants failed to further differentiate into the neuronal lineage; instead, they entered a quiescent status. This hypothesis may provide an explanation for the limited ability of the adult brain to supply neuronal loss after injury. Therefore, transcriptomic events in each subtype, detailed reprogramming lineage trajectories, and their governing factors need to be addressed.

Here, we identified DEG details and their annotated functions for each NSC & astrocyte subtype (Fig. 4D and Supplemental Table S6), creating an ideal resource for subsequent studies of mTBI pathophysiology and therapeutic targets to promote neurogenesis after brain injury. We focused on transcription factors (TFs), critical factors regulating gene expression. SCENIC analysis was used to establish a regulatory network for TFs and their downstream genes (Aibar et al. 2017) (Fig. 4E-F). We used SCENIC analysis to binarize TF enrichment and generate a regulon activity matrix (Fig. 4E). We found that TF behavior (on/off) varied across different cell clusters, which can be traced back to the subtypes characterized above. We detected 5 separate modules in the SCENIC map and listed the TFs of interest in Fig. 4E. For instance, ESRRG, RFX4, GRHL, and EPAS1 were especially active in

astrocytes and qNSCs; KLF9, GlLS3, TEF, EPAS1, and TCF7L1 were "switched on" in astrocytes, qNSCs, and early aNSCs; BRCA1, KDM5A, TAF1, and E2F1 were highly active in early aNSCs; and FOXP2, PBX3, and SOX4 were enriched in late aNSC and neuroblasts (Fig. 4E). In addition, we found that most DEGs were regulated by a combination of TFs, thus forming various regulatory networks grouped in different modules (Fig. 4G). Particularly, we found that the *Tcf7l1*, which was enriched in astrocytes, qNSC and early aNSC (Fig. 4F), has been demonstrated to maintain spinal cord precocious progenitor population by inhibiting its differentiation (Kim and Dorsky 2011).

We hypothesize that the *Tcf7l1* might play a similar differentiation-inhibiting role in subsets of SVZ NSCs as well. Consequently, in the downstream investigation, we explored this potential function of *Tcf7l1* in NSC differentiation and neurogenesis. In summary, our study revealed the significant heterogeneities among SVZ NSCs in response to mTBI, and these responses were regulated by a complex network of TFs. Elucidating the roles of these key genes may facilitate the recovery of brain tissues.

To elucidate the reprogramming lineage trajectories and their governing factors under each condition, we used Monocle2 to uncover and exhibit pseudo-time trajectory ordering of all NSC & astrocyte subtypes (Fig. 5A). 5 states were detected along the route, with 2 bifurcations: branch 1 from state 1 to states 2 and 5, and branch 2 from state 2 to states 3 and 4 (Fig. 5C). We

plotted the cell types against pseudotime and found that niche astrocytes took up the tip of the pseudo-time tree (state 1) (Fig. 5B), indicating that niche astrocyte priming may be the initial event of neurogenesis. This result challenges the traditional notion of neurogenesis, but agrees with a recent study on striatal astrocytes, which showed that astrocytes were located upstream of NSCs in the neuronal lineage and may be targeted to guide neuronal differentiation (Magnusson et al. 2020). Further experimental validation and more scientific evidence are required to clarify this issue. This process was followed by qNSC expansion (states 2 and 5) (Fig. 5B). Upon branching, the vast majority of early aNSCs formed the end of state 2 and dormant state 4. Another small group of early aNSCs gradually developed into late aNSCs and then into neuroblasts (Fig. 5B). During this period, the mTBI group exhibited an almost 10% decrease in the number of cells in state 3, suggesting limited differentiation towards late aNSCs and neuroblasts (Fig. 5D). The changes in cell type proportions have been validated using scCODA tool (Buttner et al. 2021) (Supplemental Table S3). This might partially explain why the newly generated neurons in the adult brain is insufficient to fully compensate for the loss of neurons caused after the injury.

To identify the factors and targets that govern neurogenesis, we analyzed gene expression patterns along the reprogramming trajectories and grouped them into 3 clusters according to their expression dynamics (Fig. 5E). Genes responsible for NSC proliferation, differentiation, and neuronal function

exhibited largely different expression when cell identity switched from early aNSCs to late aNSCs and neuroblasts (Fig. 5E). These changes included genes involved in "nuclear division," "axonogenesis," "dendrite development," "regulation of neurogenesis," and "neuron projection guidance" (Fig. 5E). In addition, NSC maintenance factors, such as genes from the "Hippo signaling pathways," "Rap1 signaling pathways," and "Wnt signaling pathways," increased in certain remaining qNSCs, which might underlie their maintained cell fate (Fig. 5E). *Tcf7l1, Fars2*, *Wdr17, Csmd1*, *Prex2*, *Adamts18, Erbb4, Maml3*, and *Nrxn3* exhibited varying degrees of increase or decline during aNSC differentiation to neuroblasts (Fig. 5F). Considering the aforementioned alterations of the regulon *Tcf7l1*, we are strongly interested in its role in neurogenesis following mTBI.

*Inhibiting Tcf7l1 in NSCs Promoted Differentiation towards the Neuronal Lineage*

Based on the above findings, as well as literature reviewing (Kim and Dorsky 2011), we hypothesized that *Tcf7l1* might play a differentiation-inhibiting role in subsets of SVZ-NSC. To investigate this, we employed the loss-of-function method to study the function of *Tcf7l1* in NSCs through siRNA-induced *Tcf7l1* knockdown (KD) in NE-4C cells (an immortalized mouse NSC line) (Fig. 6A). After validating the KD efficiency (Fig. 6B-C), we harvested NE-4C cells at different time points following *Tcf7l1*_siRNA treatment (1 day and 3 days) and analyzed gene expression. *Tcf7l1* deficiency decreased the expression of

315 marker genes for qNSCs (*Blbp*) and early aNSCs (*Adamts18* and *Cd9*) and
316 augmented the neuronal lineage markers *Dcx* and *Meg3* and the late aNSC
317 marker *Egfr*, suggesting differentiation towards late aNSCs and neuroblasts
318 (Fig. 6D and Supplemental Fig S4C). We further verified the gene expression
319 results using immunofluorescence staining (Fig. 6E-F). Consistently, the
320 qNSC marker *Thbs4* decreased, and the neuronal lineage marker *Dcx*
321 increased after KD. Furthermore, *Tcf7l1*-deficient cells gathered together in a
322 neurosphere-like manner. This morphological change has also been observed
323 in previous investigations of neuronal differentiation from NSCs (Fig. 6E-F).
324 Overall, these results suggest that *Tcf7l1* is critical in maintaining cell
325 stemness, and *Tcf7l1* deficiency could change the NSC programming trajectory,
326 promoting differentiation towards neuronal lineage cells.

327 *Targeting Tcf7l1 Enhanced Neurogenesis Following mTBI*

328 To further validate the critical role of *Tcf7l1*, we performed *Tcf7l1*-KD in an
329 experimental mouse model of mTBI. We stereotactically injected adenoviruses
330 loaded with vectors encoding green fluorescent protein (GFP) and scrambled
331 sh-*Tcf7l1* into the SVZ of mice 3 days before mTBI (Fig. 7A). On the third day
332 after mTBI, the mice were euthanized and the SVZ was dissected (Fig. 7A).
333 GFP signals were observed in a large number of cells in the SVZ niche,
334 suggesting successful injection and viral infection of the SVZ (Fig. 7B). *In vivo*
335 *Tcf7l1*-KD was validated via gene expression analysis of the SVZ (Fig. 7C).
336 Immunostaining revealed a significantly increased ratio of MKI67 and THBS4

co-stained/THBS4-positive cells in the SVZ after mTBI, further elevated in mTBI mice pre-treated for *Tcf7l1*-KD. These results suggest that mTBI promoted aNSC proliferation in this neurogenic niche, and suppressing THBS4 augmented this alteration (Fig. 7D-E). Notably, the total number of aNSCs (indicated as THBS4+) did not change significantly under *Tcf7l1*-KD following mTBI. Overall, the above results raised the question whether TCF7L1 deficiency promotes the differentiation of proliferated aNSCs towards their descendants. To trace the fate of these proliferated cells, we treated mice with BrdU injections for five consecutive days after mTBI and co-stained BrdU with Dcx (Fig. 7A & 7F). We observed a significant increase in the percentage of $BrdU^+$ and $DCX+/BrdU^+$ in the mTBI+*Tcf7l1*-KD group, suggesting that neuronal lineage differentiation of proliferated NSCs is enhanced under TCF7L1 deficiency (Fig. 7G). Together, our *in vitro* and *in vivo* results demonstrate that *Tcf7l1* plays a critical role in maintaining NSC quiescence and suppressing neuronal lineage differentiation. Targeting *Tcf7l1* represents a potential direction in regenerative medicine for brain injury.

## Discussion

Through high-throughput single-cell profiling, we(1) demonstrates that our comprehensive snRNA-seq strategy generates a cell atlas of the entire SVZ niche, (2) reports significant information about the cells, genes, and pathways vulnerable to mTBI, and reveals cell-type-specific dynamics along the neurogenic lineage, (3) identifies key genes like *Tcf7l1* that have the potential

359 to ameliorate cell damage in the brain or facilitate neural repair, making them
360 potential targets for developing therapeutics for mTBI, and (4) provides a
361 resource for studying adult neurogenesis in the SVZ under both physiological
362 and pathological conditions. To support our data-driven strategy, we
363 conducted experimental validations and demonstrated, for the first time, that
364 a deficiency of the transcription factor Tcf7l1, a regulator of cell cycle genes,
365 switches the NSC reprogramming directions and promotes NSC
366 differentiation towards neuronal lineage, providing a promising target for
367 future regeneration medicine approaches.

368 Previous studies have described the processes involved in cell proliferation
369 and differentiation during neurogenesis. Recent efforts continue to unveil the
370 diversity of NSCs and progenitors harbored in the heterogeneous pool, but
371 their lineage trajectories and delicate intercellular communications remain
372 poorly understood. Utilizing single-cell technology, Llorens-Bobadilla et al.
373 unveiled distinct cell types or states within the SVZ. Their investigation
374 successfully identified four subtypes of NSCs and elucidated the factors
375 implicated in the transition of NSCs from a quiescent state to an activated
376 state under forebrain ischemia (Llorens-Bobadilla et al. 2015). Subsequently,
377 Vera Zywitza et al. characterized and classified six subtypes of NSCs in the
378 SVZ based on molecular features and RNA velocity analysis (Zywitza et al.
379 2018). Additionally, they demonstrated the pivotal role of LRP2 as a key
380 regulator of neurogenesis in the SVZ. Recently, Xie et al. conducted an

analysis on the heterogeneity of SVZ stem cells in mice across different age groups, spanning from neonates to aged individuals (Xie et al. 2020). Their study successfully identified four distinct subtypes of qNSCs and three subpopulations of progenitor cells. While these studies differ in terms of the precision in subtyping SVZ stem cells, they share similarities in classifying major NSC types such as aNSCs, qNSCs, and NBs, which aligns with the findings of our study.

Using a well-established mTBI model and single-nucleus transcriptomics, we conducted a pioneering investigation into the molecular and transcriptional alterations specific to cell types within the SVZ stem cell pool following mild brain trauma. In addition, we uncovered a number of novel genes that have the potential to mark cell type in SVZ niche and each NSC/progenitor cell subtype, thus filling this current knowledge gap. For instance, distinguishing qNSCs from niche astrocytes effectively with a specific marker has been challenging; hence, the likelihood ratio has been applied to identify them (Llorens-Bobadilla et al. 2015). Our data detected several genes exclusively enriched in qNSCs, not in niche astrocytes (Supplemental Table S5). Specifically, *Kank1* exhibited exclusive expression in qNSCs, while *Grin2c* and *Mertk* showed highly expression in astrocytes. These genes, not previously reported, offer potential markers for identifying these cell types. Another previous notion challenged by our data is that neurogenesis lineage priming is initiated by qNSC activation. Using pseudotime analysis, a powerful approach

for revealing lineage trajectories (Holden et al. 2021; Jamjoom et al. 2021), we discovered that niche astrocytes triggered the neurogenic process, rather than qNSCs. Our findings align with a recent study suggesting that striatal astrocytes act as latent NSCs, triggering neuronal lineage cell genesis upstream of NSCs (Magnusson et al. 2020). In addition, our analysis revealed that qNSCs differentiated into two branches along the pseudotime line. One branch of qNSC transitioned into a dormant state, mainly comprising early aNSCs. These cells shared similar activated TFs with astrocytes and qNSCs (Fig. 4E), suggesting that their transcriptional regulatory network did not undergo significant changes during differentiation. Another branch differentiated into late aNSCs and subsequently into neuroblasts. In comparison, this branch exhibited a completely different regulatory network (Fig. 4G), suggesting a distinct switch in cell identity. Conducting in-depth studies to validate these analytical results and further exploring targets involved in NSC homeostasis and neurogenesis would be of significant interest. Our data also offer insights into the mechanisms underlying the limited replacement of lost neurons after brain injury and potential targets to address this issue. In addition, we clarified the molecular events orchestrating each neurogenic stage at the single-cell resolution and identified potential genes that may govern the fate of each NSC/progenitor subtype. This discovery is expected to facilitate the development of regenerative medicines.

Our single-nucleus SVZ transcriptome atlas and lineage trajectory regulation

425 analysis revealed *Tcf7l1* as a key gene in NSC differentiation. Among the four
426 TCF/lymphoid enhancer factor family members, *Tcf7l1* is the only one
427 expressed in undifferentiated mouse embryonic stem cells (Yi et al. 2011) and
428 in the developing forebrain primordium during the presomitic and early
429 somite stages (Galceran et al. 1999; Merrill et al. 2004). A literature review
430 revealed that *Tcf7l1* can maintain the spinal cord precocious progenitor cell
431 population and inhibit its differentiation in zebrafish (Andoniadou et al. 2011;
432 Kim and Dorsky 2011). However, its role in the SVZ of adult mice and its
433 effects on neurorepair after mTBI have not been addressed. *In vitro* and *in*
434 *vivo loss*-of-function experiments demonstrated that suppressing *Tcf7l1*
435 promotes qNSC differentiation towards neuronal lineage cells. This
436 experiment validates our single-nucleus data-driven strategy. In addition,
437 these results aid in understanding the pathophysiological process of mTBI,
438 and our fate-switching approach represents a significant advancement in
439 neuroregeneration, offering a potential therapeutic target for enhancing
440 neuronal supply after brain injury.

441 To further explore the potential therapeutic effects of *Tcf7l1*, we conducted the
442 NSS assessment in mice 1 hour after mTBI. Mice with *Tcf7l1*-KD exhibited
443 significantly lower NSS scores compared to the mTBI group treated with a
444 control vector (Supplemental Fig S5A), indicating a reduced level of
445 neurological impairment in the *Tcf7l1*-KD group. To evaluate the long-term
446 impact of *Tcf7l1* KD in mice, we conducted additional behavioral experiments

447 on Sham, mTBI+Control vector, and mTBI+*Tcf7l1* KD mice 1 month post-
448 injury. These experiments included the Rotarod test, Morris water maze test
449 (MWM), Y-maze test, and novel object recognition test (Supplemental Fig S5).
450 In the Rotarod test, we found that the motor and coordination abilities of
451 mTBI+*Tcf7l1* KD mice were significantly better than those of mTBI+Control
452 vector group in the first 3 trials (Supplemental Fig S5B). From the 2nd day
453 onwards (after the 4th trial), there was no significant difference among the 2
454 groups. The Y-maze test results showed that the spontaneous alternation rate
455 of mTBI+*Tcf7l1* KD mice was significantly higher than that of mTBI+Control
456 vector mice 1 month after injury (Supplemental Fig S5C). The MWM results
457 showed that the latency of mTBI+*Tcf7l1* KD mice on the 4th and 5th days was
458 significantly shorter than that of mTBI+Control vector mice, and their overall
459 spatial learning and localization abilities were close to those of Sham mice
460 (Supplemental Fig S5D). In the spatial exploration, mTBI+*Tcf7l1* KD mice
461 explored the quadrant where the original platform was located for a longer
462 time than mTBI+Control vector mice, but the difference was not significant
463 (Supplemental Fig S5E). The novel object recognition test showed that there
464 was no significant difference among the groups of mice in exploring old
465 objects, but mTBI+*Tcf7l1* KD mice spent significantly more time exploring
466 new objects than mTBI+Control vector mice (Supplemental Fig S5F). The
467 above results indicate that mTBI+*Tcf7l1* KD mice have better motor, memory,
468 and learning abilities than mTBI+Control vector mice 1 month after injury.

However, it's essential to acknowledge that the transition from SVZ neurogenesis to cognitive function in post-TBI mice is a complex and multifaceted process. This journey involves not only the proliferation and differentiation of NSCs, but also the migration of neural cells, the establishment of the surrounding micro-environment, and the construction of neural circuits. Consequently, confirming a direct causal relationship between the enhancement of cognitive function and SVZ neurogenesis regulated by Tcf7l1 would necessitate a considerable volume of subsequent and comprehensive studies. As such, we recognize that further research is required to fully unravel the exact mechanisms that underpin the observed enhancements in cognitive function.

Acknowledging the limitations of our study is imperative. It has been observed that following TBI, female animals experience an elevation in estrogen levels at the site of trauma, which is potential to mitigate neuroinflammatory responses mediated by microglia and astrocytes (Wang et al. 2020). This increase in estrogen plays a vital role in reducing intracranial pressure and mitigating brain edema, ultimately leading to a better prognosis (Brotfain et al. 2016; Lu et al. 2017). Consequently, many studies investigating brain injury opt to restrict the use of mice to a specific sex in order to minimize variability and eliminate the influence of sex hormones on experimental outcomes (Llorens-Bobadilla et al. 2015; Arneson et al. 2018; Park et al. 2018; Somebang et al. 2021). In the present study, in order to observe the molecular

level changes after mTBI more clearly, we have solely utilized male mice for single-nucleus sequencing, which inherently restricts our ability to draw conclusions regarding potential sex disparities in response to mTBI. Thus, we have outlined future research directions that include conducting comparative studies between male and female mice using the single-cell transcriptomic approach to investigate sex-specific differences in mTBI response. We firmly believe that such investigations will yield valuable insights into the underlying mechanisms of sex disparities in mTBI and provide guidance for potential sex-specific therapeutic interventions.

## Methods

*Ethics approval and consent to participate*

Animal experiments were carried out in accordance with the institutional guidelines approved by the Animal Care and Experimental Committee of Sichuan University, China.

*Animals*

All animal experiments were carried out in accordance with the institutional guidelines following approval by the Animal Care and Experimental Committee of Sichuan University, China. C57BL/6J male mice, aged 8-10 weeks, were group-housed conventionally in standard conditions (12 hrs light/dark cycle, temperature: 22-25 °C, relative humidity: 40-60%) with ad libitum food and water for at least one week before the experiment. To ensure proper blinding, each mouse was assigned a unique alphanumeric code

unrelated to the treatment group for identification purposes. For NSS assessment and single-cell sequencing, a total of 6 SVZ samples were utilized. In the in vivo experiments, a cohort of 60 mice was employed, with 20 mice allocated to each respective group. These mice underwent immunofluorescence staining, BrdU injection, and behavioral testing procedures. The study implemented specific exclusion criteria for mouse selection in subsequent experimentation. Mice meeting any of the following criteria were excluded: 1) age below 8 weeks or above 10 weeks, 2) body weight below 18 grams or above 25 grams, 3) presence of illness or disease, 4) technical issues during experimental procedures, 5) specific breeding or housing conditions introducing confounding variables or impacting study outcomes, 6) prior treatments or interventions, and 7) certain genetic or phenotypic backgrounds.

*mTBI*

To ensure consistent and standardized anesthesia, we employed an inhalation anesthesia machine with isoflurane for our study as isoflurane anesthesia offers advantages such as rapid induction and recovery (Bielefeld et al. 2017; Cho et al. 2019; Huynh et al. 2020). Mice were anesthetized with 4% isoflurane and maintained anesthesia with 1.5% isoflurane until after impact and suturing. Mice were placed in an anesthetic mask and a stereotaxic apparatus, with a foam pad placed underneath to provide cushioning for the

impact (Xu et al. 2016). First, a 10 mm midline incision was made in the mouse's scalp and the skin and the fascia were cleared. Then mice received an impact by the CCI machine eCCI-6.3 (Custom Design & Fabrication, Inc.) directly onto the skull, with an impact diameter of 3 mm, impact velocity of 3.5 m/s, depth of 1 mm, and duration of 150 ms. The impact position was 0.5 mm posterior to the bregma and 2 mm lateral to the midplane. These injury parameters are consistent with those used in previous studies of mTBI (An et al. 2016; Xu et al. 2021). The sham group of mice did not receive an impact, but were otherwise treated identically to the mTBI group.

*NSS*

We used the NSS assessment to validate the severity of brain injury in mice 1 hr post injury as previously described in detail (Flierl et al. 2009). The NSS evaluation comprises a comprehensive range of assessments to evaluate neurological function, encompassing motor coordination, balance, and reflexes. According to the established criteria (Beni-Adani et al. 2001), a score of 3-4 was considered indicative of mTBI (Henninger et al. 2016). According to the NSS protocol in Flierl et al.'s work, the mice were exposed to isoflurane inhalation for a limited duration of 5-10 minutes to prevent prolonged interference with NSS evaluation. To demonstrate that mice are fully awake from the anesthetic state 1 hour after injury, we conducted an NSS comparison between mice that received anesthesia-only and naive mice

(Supplemental Fig S5A). The results clearly demonstrated that the NSS scores of anesthetized mice at 1 hour post-TBI were comparable to those of naive mice, indicating no significant differences in neurological function.

*Intracranial injections, immunofluorescence staining, real-time quantitative polymerase chain reaction (qPCR)*

Please refer to our previous publications (Xiao et al. 2019; Cao et al. 2022; Long et al. 2022).

Antibodies: anti-Thbs4 (Abcam Cat# ab263898, RRID: AB_2922811), anti-Dcx (Abcam Cat# ab207175, RRID: AB_2894710), anti-Ki67 (Abcam Cat# ab279653, RRID: AB_2934265).

Primer sequences: please see Supplemental Table S7.

*BrdU injection and immunostaining*

We initiated BrdU injections immediately after mTBI and continued daily injections for 5 consecutive days to label proliferative cells. Mice were received daily single i.p. injections of BrdU (Abcam, Cat# ab142567, 50 mg/kg). Sections were incubated with 2 N HCl for 1 hour before immunostaining against BrdU (Thermo Fisher Scientific Cat# MA3-071, RRID: AB_10986341).

*SVZ dissection*

Please refer to previous study (Kim and Dorsky 2011; Li et al. 2023).

*Nuclei isolation*

The mice SVZ was dissected according to previous study (Walker and

Kempermann 2014). NLB buffer (0.2 U/μL RNase Inhibitor (Takara), 250 mM Sucrose, 10 mM Tris-HCl, 3 mM MgAc2, 0.1% Triton X-100 (Sigma-Aldrich), 0.1 mM EDTA) was used to homogenize the frozen tissue. Different concentrations of sucrose were applied to purify the nuclei using sucrose density gradient centrifugation, and the nuclei were inspected for visual appearance and cell lysis using trypan blue and quantified with a hemocytometer before being adjusted to a concentration of 1000 nuclei/μL.

*Single nucleus RNA sequencing*

The snRNA-seq libraries were built using the 10× Genomics Chromium Controller Instrument (Cat# PN-120223, 10 × Genomics) and Chromium Single Cell 3' V3.1 Reagent Kits (Cat# PN-1000121, 10× Genomics). Please refer to manufacturer's instructions.

*Cell culture and transfection*

NE4C cell line were cultured in a 37 °C incubator under 5% $CO_2$ with Dulbecco's Modified Eagle Medium (DMEM) containing 10% fetal bovine serum and 1% double antibody. For transfection, cells were transfected with siRNA-Tcf7l1 or the control siRNA using Lipofectamine 3000 according to the manufacturer's instructions. Briefly, 250 pmole of each siRNA were transfected using 2.5 μl of lipofectamine 2000 per dish in Opti-MEM. Following transfection, cells were incubated at 37 °C in a 5% CO2 humidified atmosphere for 48 h before being harvested for the assays. The sequences

corresponding to the siRNA-Tcf7l1 were: sense 5'-GGAAGAAGAAGAAGAGGAAGAGAGA-3'.

*Single nucleus RNA sequencing quality control*

Expression matrixes were loaded into R (v.4.1.3) using the function Read10× in Seurat (v.1.1) (Stuart et al. 2019; R Core Team YEAR) and then merged together by column (detailed dataset descriptions of the sham group has been reported in our recent data descriptor, https://www.ncbi.nlm.nih.gov/geo/query/acc.cgi?acc=GSE198074) (Li et al. 2023). This resulted in total of 16,754 cells. We performed quality control to remove doublets, dead cells, and empty droplets that could impact the accuracy and reliability of our sequencing results. The quality control criteria are as follows: (1) 1,000 < total UMI counts < 20,000; (2) 500 < gene numbers < 7,500; and (3) mitochondrial gene percentage < 10%. After attempts of quality control, we filtered out 1489 low-quality cells that did not meet our filtering criteria for analysis. This step was crucial in ensuring the quality of our data and minimizing any potential sources of bias or artifacts in our analysis. The expression level of each gene in each cell was normalized using the function NormalizeData with the default parameters to remove the influence of sequencing library size, which converted expression values from UMI counts to ln[10,000 × UMI counts/total UMI counts in cell + 1]. The Seurat R package (v4.1.1) and SCTransform (v0.2.1) R packages were used for the downstream analysis of single-cell RNA-seq data (Hafemeister and Satija

2019; Stuart et al. 2019). Briefly, the expression matrix was processed using SCTransform with default parameters, followed by dimensionality reduction (PCA, principal component analysis). Then, clusters were visualized using Uniform Manifold Approximation and Projection for Dimension Reduction (UMAP). Cell clustering was further performed using the FindNeighbors and FindClusters functions in Seurat. Cell populations were defined based on the DEGs identified between clusters.

*Marker gene identification*

Marker genes were identified with a Wilcoxon rank sum test implemented in the FindAllMarkers function with the criteria (logFC>0.25; p<0.05; min.pct>0.1). The expression of single genes was depicted using custom R scripts, either per cell cluster as distribution of normalized UMI counts (violins) or per cell as color gradient in UMAP.

*Functional annotation and pathway Analysis*

Gene Ontology (GO) annotations (The Gene Ontology Consortium et al. 2000) were downloaded from NCBI (http://www.ncbi.nlm.nih.gov/), GO knowledgebase (http://www.geneontology.org/), and UniProt (http://www.uniprot.org/). Pathway analysis was performed using the KEGG database (https://www.genome.jp/kegg/). Fisher's exact test was applied to identify significant GO categories and pathways. False Discovery Rate (FDR) was used to correct the p-values, and p-values < 0.05 were considered

significant (Draghici et al. 2007).

*Cell-Cell communication analysis*

Communications between cells were analyzed using CellChat (Jin et al. 2021). Please refer to https://github.com/sqjin/CellChat. P-values < 0.05 were selected for revealing relationships between cell types.

*Single-cell regulatory network inference and clustering (SCENIC)*

For SCENIC (Aibar et al. 2017), we created the motif databases the allow to use RcisTarget and SCENIC (v1.3.1) on mouse. Briefly, we used GENIE3 to construct co-expression network and RcisTarget to identify the direct binding by DNA-motif analysis. After construct regulons for each transcription factor using motif data set (mm9-tss-centered-10kb-7-species.mc9nr.feather, mm10-refseq-r80-500bp-up-and-100bp-down-tss.mc9nr.feather), the activity score of the regulons in each cell was quantified using AUCell. The activity scores of regulons generated in NSC & astrocyte in mTBI and control mice were averaged, scaled, and visualized via heat map. The network of the regulon and its targets was visualized using Cytoscape (v3.8.0) (Shannon et al. 2003). Only the connections of a specific regulon and downstream Targets that were co-regulated by multiple TF were shown.

*Pseudo-time analysis*

The reprogramming trajectory analysis was performed using Monocle2 (v2.22.0, http://cole-trapnell-lab.github.io/monocle-release), with DDR-Tree

(v0.1.5) and default parameters. A heatmap was produced to display the series of genes with certain expression patterns along the pseudotime. Using the differential gene test function of Monocle2, a q value <0.01 was set to identify significantly changed genes.

*scCODA*

To identify statistically significant changes in cell population composition, we utilized the scCODA v.0.1.9 Python package to perform compositional analysis of the single-cell data (Buttner et al. 2021). For Fig. 2A, Fig. 4C, and Fig. 5D, we selected ependymal, astrocyte, and State1 cells as the reference cell types, respectively. To ensure the detection of subtle yet biologically relevant changes, we set the FDR value to 0.4, as recommended by Buttner et al. in their documentation.

*Statistical analyses*

The data analysis was carried out by a blinded investigator, unaware of the treatment groups. The data were labeled with unique alphanumeric codes, unlinked to the treatment groups. In the statistical analysis, FDR was employed to correct the p-values. We defined p-values < 0.05 as significant. The p-values are reported in the figures, figure legends (*p <= 0.05, ** <= 0.01, ***p <= 0.001, ****p <= 0.0001, n.s. denotes not significant). The error bars in the figures represent the mean ± SEM. For the statistical analysis of snRNA-seq data, we utilized R (v4.1.3). The Wilcoxon rank sum test was

utilized for marker gene identification, as well as for the selection of DEGs for pseudo-time analysis, cell-cell communication analysis, and other related analyses. Fisher's exact test was applied to identify significant GO categories and pathways. Additionally, the *t*-test was employed to determine statistical differences between samples. Detailed analysis methods and relevant parameter indicators have been described aforementioned. For NSS, qPCRs, and immunostaining statistic data, we performed unpaired two-tailed *t*-tests using GraphPad Prism (v.8.0) to determine statistical differences between samples.

## Data access

All raw and processed sequencing data of mTBI generated in this study have been submitted to the NCBI Gene Expression Omnibus (GEO; https://www.ncbi.nlm.nih.gov/geo/query/acc.cgi?acc=GSE198074) under accession number GSE198074. The analysis code is available at GitHub (https://github.com/limanrui/scseq.git) and as Supplemental Code. Matrix of samples in this study are available at Figshare (https://doi.org/10.6084/m9.figshare.21907497.v2) and as Supplemental Data.

## Competing interests statement

The authors declare that they have no competing interests.

## Acknowledgements

The study was funded by the National Natural Science Foundation of China to Xiameng Chen (No. 82202077) and the Natural Science Foundation of Sichuan Province to Xiameng Chen (No. 23NSFSC4762).

## Authors' contributions

Q.Y., Lingxuan.Z., Manrui.L., Y.X., Xiaogang.C and R.Y. performed the statistical and computational analysis. X.O., M.H. and Miao.L performed CCI and tissue sampling. Q.Y., Lingxuan.Z., Manrui.L., Y.X., and H.D. performed the PCR validation, immunofluorescence staning, cell counting and SVZ injection. Q.Y. and Xiameng.C. wrote the manuscript. Lin.Z., Xiaogang.C. and Meili.L. revised the manuscript. The study was designed and managed by Xiameng.C., W.L., and X.X.

## References

Aibar S, Gonzalez-Blas CB, Moerman T, Huynh-Thu VA, Imrichova H, Hulselmans G, Rambow F, Marine JC, Geurts P, Aerts J et al. 2017. SCENIC: single-cell regulatory network inference and clustering. *Nat Methods* **14**: 1083-1086.

An C, Jiang X, Pu H, Hong D, Zhang W, Hu X, Gao Y. 2016. Severity-Dependent Long-Term Spatial Learning-Memory Impairment in a Mouse Model of Traumatic Brain Injury. *Transl Stroke Res* **7**: 512-520.

Andoniadou CL, Signore M, Young RM, Gaston-Massuet C, Wilson SW, Fuchs E, Martinez-Barbera JP. 2011. HESX1- and TCF3-mediated repression of Wnt/beta-catenin targets is required for normal development of the anterior forebrain. *Development* **138**: 4931-4942.

Arneson D, Zhang G, Ying Z, Zhuang Y, Byun HR, Ahn IS, Gomez-Pinilla F, Yang X. 2018. Single cell molecular alterations reveal target cells and pathways of concussive brain injury. *Nat Commun* **9**: 3894.

Barreto GE, Gonzalez J, Torres Y, Morales L. 2011. Astrocytic-neuronal crosstalk: implications for neuroprotection from brain injury. *Neurosci Res* **71**: 107-113.

Batiuk MY, Martirosyan A, Wahis J, de Vin F, Marneffe C, Kusserow C, Koeppen J, Viana JF, Oliveira JF, Voet T et al. 2020. Identification of region-specific astrocyte subtypes at single cell resolution. *Nature Communications* **11**.

734 Beckervordersandforth R, Tripathi P, Ninkovic J, Bayam E, Lepier A, Stempfhuber B,
735 Kirchhoff F, Hirrlinger J, Haslinger A, Lie DC et al. 2010. In vivo fate mapping and
736 expression analysis reveals molecular hallmarks of prospectively isolated adult neural
737 stem cells. *Cell Stem Cell* **7**: 744-758.
738 Beni-Adani L, Gozes I, Cohen Y, Assaf Y, Steingart RA, Brenneman DE, Eizenberg O,
739 Trembolver V, Shohami E. 2001. A peptide derived from activity-dependent
740 neuroprotective protein (ADNP) ameliorates injury response in closed head injury in
741 mice. *J Pharmacol Exp Ther* **296**: 57-63.
742 Biancalani T, Scalia G, Buffoni L, Avasthi R, Lu Z, Sanger A, Tokcan N, Vanderburg CR,
743 Segerstolpe A, Zhang M et al. 2021. Deep learning and alignment of spatially resolved
744 single-cell transcriptomes with Tangram. *Nat Methods* **18**: 1352-1362.
745 Bielefeld P, Sierra A, Encinas JM, Maletic-Savatic M, Anderson A, Fitzsimons CP. 2017. A
746 Standardized Protocol for Stereotaxic Intrahippocampal Administration of Kainic
747 Acid Combined with Electroencephalographic Seizure Monitoring in Mice. *Front*
748 *Neurosci* **11**: 160.
749 Brotfain E, E. Gruenbaum S, Boyko M, Kutz R, Zlotnik A, Klein M. 2016. Neuroprotection by
750 Estrogen and Progesterone in Traumatic Brain Injury and Spinal Cord Injury.
751 *Current Neuropharmacology* **14**: 641-653.
752 Bu W, Ren H, Deng Y, Del Mar N, Guley NM, Moore BM, Honig MG, Reiner A. 2016. Mild
753 Traumatic Brain Injury Produces Neuron Loss That Can Be Rescued by Modulating
754 Microglial Activation Using a CB2 Receptor Inverse Agonist. *Front Neurosci* **10**: 449.
755 Buono KD, Vadlamuri D, Gan Q, Levison SWJDn. 2012. LIF is Essential for SVZ Neural Stem
756 Cell and Progenitor Homeostasis as Revealed by a Novel Flow Cytometric Analysis.
757 **34**: 449.
758 Buttner M, Ostner J, Muller CL, Theis FJ, Schubert B. 2021. scCODA is a Bayesian model for
759 compositional single-cell data analysis. *Nat Commun* **12**: 6876.
760 Cao Q, Benton RL, Whittemore SR. 2002. Stem cell repair of central nervous system injury.
761 *Journal of neuroscience research* **68**: 501-510.
762 Cao S, Li M, Sun Y, Wu P, Yang W, Dai H, Guo Y, Ye Y, Wang Z, Xie X et al. 2022.
763 Intermittent fasting enhances hippocampal NPY expression to promote neurogenesis
764 after traumatic brain injury. *Nutrition* **97**: 111621.
765 Chavali M, Klingener M, Kokkosis AG, Garkun Y, Felong S, Maffei A, Aguirre A. 2018. Non-
766 canonical Wnt signaling regulates neural stem cell quiescence during homeostasis
767 and after demyelination. *Nature communications* **9**: 1-17.
768 Chiu CC, Liao YE, Yang LY, Wang JY, Tweedie D, Karnati HK, Greig NH, Wang JY. 2016.
769 Neuroinflammation in animal models of traumatic brain injury. *J Neurosci Methods*
770 **272**: 38-49.
771 Cho C, Michailidis V, Lecker I, Collymore C, Hanwell D, Loka M, Danesh M, Pham C, Urban P,
772 Bonin RP et al. 2019. Evaluating analgesic efficacy and administration route following
773 craniotomy in mice using the grimace scale. *Sci Rep* **9**: 359.
774 Collins-Praino LE, Arulsamy A, Katharesan V, Corrigan F. 2018. The effect of an acute
775 systemic inflammatory insult on the chronic effects of a single mild traumatic brain
776 injury. *Behavioural brain research* **336**: 22-31.
777 Doetsch F, Caille I, Lim DA, García-Verdugo JM, Alvarez-Buylla AJC. 1999. Subventricular

zone astrocytes are neural stem cells in the adult mammalian brain. **97**: 703-716.
Dougherty KJ, Zagoraiou L, Satoh D, Rozani I, Doobar S, Arber S, Jessell TM, Kiehn O. 2013. Locomotor rhythm generation linked to the output of spinal shox2 excitatory interneurons. *Neuron* **80**: 920-933.
Draghici S, Khatri P, Tarca AL, Amin K, Done A, Voichita C, Georgescu C, Romero R. 2007. A systems biology approach for pathway level analysis. *Genome Res* **17**: 1537-1545.
Flierl MA, Stahel PF, Beauchamp KM, Morgan SJ, Smith WR, Shohami E. 2009. Mouse closed head injury model induced by a weight-drop device. *Nat Protoc* **4**: 1328-1337.
Furtado ABV, Goncalves DF, Hartmann DD, Courtes AA, Cassol G, Nunez-Figueredo Y, Argolo DS, do Nascimento RP, Costa SL, da Silva VDA et al. 2021. JM-20 Treatment After Mild Traumatic Brain Injury Reduces Glial Cell Pro-inflammatory Signaling and Behavioral and Cognitive Deficits by Increasing Neurotrophin Expression. *Mol Neurobiol* **58**: 4615-4627.
Galceran J, Farinas I, Depew MJ, Clevers H, Grosschedl R. 1999. Wnt3a-/--like phenotype and limb deficiency in Lef1(-/-)Tcf1(-/-) mice. *Genes Dev* **13**: 709-717.
Hafemeister C, Satija R. 2019. Normalization and variance stabilization of single-cell RNA-seq data using regularized negative binomial regression. *Genome Biol* **20**: 296.
Henninger N, Bouley J, Sikoglu EM, An J, Moore CM, King JA, Bowser R, Freeman MR, Brown RH, Jr. 2016. Attenuated traumatic axonal injury and improved functional outcome after traumatic brain injury in mice lacking Sarm1. *Brain* **139**: 1094-1105.
Holden SS, Grandi FC, Aboubakr O, Higashikubo B, Cho FS, Chang AH, Forero AO, Morningstar AR, Mathur V, Kuhn LJ et al. 2021. Complement factor C1q mediates sleep spindle loss and epileptic spikes after mild brain injury. *Science* **373**: eabj2685.
Huynh LM, Burns MP, Taub DD, Blackman MR, Zhou J. 2020. Chronic Neurobehavioral Impairments and Decreased Hippocampal Expression of Genes Important for Brain Glucose Utilization in a Mouse Model of Mild TBI. *Front Endocrinol (Lausanne)* **11**: 556380.
Jamjoom AAB, Rhodes J, Andrews PJD, Grant SGN. 2021. The synapse in traumatic brain injury. *Brain* **144**: 18-31.
Jin S, Guerrero-Juarez CF, Zhang L, Chang I, Ramos R, Kuan CH, Myung P, Plikus MV, Nie Q. 2021. Inference and analysis of cell-cell communication using CellChat. *Nat Commun* **12**: 1088.
Kim H, Cho B, Park H, Kim J, Kim S, Shin J, Lengner CJ, Won KJ, Kim J. 2022. Dormant state of quiescent neural stem cells links Shank3 mutation to autism development. *Mol Psychiatry* **27**: 2751-2765.
Kim HS, Dorsky RI. 2011. Tcf7l1 is required for spinal cord progenitor maintenance. *Dev Dyn* **240**: 2256-2264.
Li M, Chen X, Yang Q, Cao S, Wyler S, Yuan R, Zhang L, Liao M, Lv M, Wang F et al. 2023. Single-nucleus profiling of adult mice sub-ventricular zone after blast-related traumatic brain injury. *Sci Data* **10**: 13.
Llorens-Bobadilla E, Zhao S, Baser A, Saiz-Castro G, Zwadlo K, Martin-Villalba A. 2015. Single-Cell Transcriptomics Reveals a Population of Dormant Neural Stem Cells that Become Activated upon Brain Injury. *Cell Stem Cell* **17**: 329-340.
Long X, Yang Q, Qian J, Yao H, Yan R, Cheng X, Zhang Q, Gu C, Gao F, Wang H et al. 2022.

Obesity modulates cell-cell interactions during ovarian folliculogenesis. *iScience* **25**: 103627.

Lu H, Ma K, Jin L, Zhu H, Cao R. 2017. 17β□estradiol rescues damages following traumatic brain injury from molecule to behavior in mice. *Journal of Cellular Physiology* **233**: 1712-1722.

Luo J, Elwood F, Britschgi M, Villeda S, Zhang H, Ding Z, Zhu L, Alabsi H, Getachew R, Narasimhan R et al. 2013. Colony-stimulating factor 1 receptor (CSF1R) signaling in injured neurons facilitates protection and survival. *J Exp Med* **210**: 157-172.

Luo Y, Coskun V, Liang A, Yu J, Cheng L, Ge W, Shi Z, Zhang K, Li C, Cui Y et al. 2015. Single-cell transcriptome analyses reveal signals to activate dormant neural stem cells. *Cell* **161**: 1175-1186.

Magnusson JP, Zamboni M, Santopolo G, Mold JE, Barrientos-Somarribas M, Talavera-Lopez C, Andersson B, Frisen J. 2020. Activation of a neural stem cell transcriptional program in parenchymal astrocytes. *Elife* **9**.

Matson KJE, Russ DE, Kathe C, Hua I, Maric D, Ding Y, Krynitsky J, Pursley R, Sathyamurthy A, Squair JW et al. 2022. Single cell atlas of spinal cord injury in mice reveals a pro-regenerative signature in spinocerebellar neurons. *Nat Commun* **13**: 5628.

Merrill BJ, Pasolli HA, Polak L, Rendl M, Garcia-Garcia MJ, Anderson KV, Fuchs E. 2004. Tcf3: a transcriptional regulator of axis induction in the early embryo. *Development* **131**: 263-274.

Mizrak D, Levitin HM, Delgado AC, Crotet V, Yuan J, Chaker Z, Silva-Vargas V, Sims PA, Doetsch F. 2019. Single-Cell Analysis of Regional Differences in Adult V-SVZ Neural Stem Cell Lineages. *Cell Rep* **26**: 394-406 e395.

Mychasiuk R, Farran A, Esser MJ. 2014. Assessment of an experimental rodent model of pediatric mild traumatic brain injury. *Journal of neurotrauma* **31**: 749-757.

Park J, Shrestha R, Qiu C, Kondo A, Huang S, Werth M, Li M, Barasch J, Susztak K. 2018. Single-cell transcriptomics of the mouse kidney reveals potential cellular targets of kidney disease. *Science* **360**: 758-763.

Pluchino S, Nicaise AM. 2021. NSCs: Sentinel Cells of the Brain. *Cell Stem Cell* **28**: 177-179.

R Core Team. YEAR. R : A Language and Environment for Statistical Computing.

Seshadri S, Kamiya A, Yokota Y, Prikulis I, Kano S, Hayashi-Takagi A, Stanco A, Eom TY, Rao S, Ishizuka K et al. 2010. Disrupted-in-Schizophrenia-1 expression is regulated by beta-site amyloid precursor protein cleaving enzyme-1-neuregulin cascade. *Proc Natl Acad Sci U S A* **107**: 5622-5627.

Shah PT, Stratton JA, Stykel MG, Abbasi S, Sharma S, Mayr KA, Koblinger K, Whelan PJ, Biernaskie J. 2018. Single-Cell Transcriptomics and Fate Mapping of Ependymal Cells Reveals an Absence of Neural Stem Cell Function. *Cell* **173**: 1045-1057 e1049.

Shannon P, Markiel A, Ozier O, Baliga NS, Wang JT, Ramage D, Amin N, Schwikowski B, Ideker T. 2003. Cytoscape: a software environment for integrated models of biomolecular interaction networks. *Genome Res* **13**: 2498-2504.

Silverberg ND, Duhaime A-C, Iaccarino MA. 2020. Mild traumatic brain injury in 2019-2020. *JAMA* **323**: 177-178.

Somebang K, Rudolph J, Imhof I, Li L, Niemi EC, Shigenaga J, Tran H, Gill TM, Lo I, Zabel BA et al. 2021. CCR2 deficiency alters activation of microglia subsets in traumatic

brain injury. *Cell Rep* **36**: 109727.

Stuart T, Butler A, Hoffman P, Hafemeister C, Papalexi E, Mauck WM, 3rd, Hao Y, Stoeckius M, Smibert P, Satija R. 2019. Comprehensive Integration of Single-Cell Data. *Cell* **177**: 1888-1902 e1821.

The Gene Ontology Consortium, Ashburner M, Ball CA, Blake JA, Botstein D, Butler H, Cherry JM, Davis AP, Dolinski K, Dwight SS et al. 2000. Gene ontology: tool for the unification of biology. The Gene Ontology Consortium. *Nat Genet* **25**: 25-29.

Volterra A, Meldolesi J. 2005. Astrocytes, from brain glue to communication elements: the revolution continues. *Nat Rev Neurosci* **6**: 626-640.

Walker TL, Kempermann G. 2014. One Mouse, Two Cultures: Isolation and Culture of Adult Neural Stem Cells from the Two Neurogenic Zones of Individual Mice. *Journal of Visualized Experiments* doi:10.3791/51225.

Wang J, Hou Y, Zhang L, Liu M, Zhao J, Zhang Z, Ma Y, Hou W. 2020. Estrogen Attenuates Traumatic Brain Injury by Inhibiting the Activation of Microglia and Astrocyte-Mediated Neuroinflammatory Responses. *Molecular Neurobiology* **58**: 1052-1061.

Wyss-Coray T. 2006. Inflammation in Alzheimer disease: driving force, bystander or beneficial response? *Nat Med* **12**: 1005-1015.

Xiao X, Jiang Y, Liang W, Wang Y, Cao S, Yan H, Gao L, Zhang L. 2019. miR-212-5p attenuates ferroptotic neuronal death after traumatic brain injury by targeting Ptgs2. *Mol Brain* **12**: 78.

Xie XP, Laks DR, Sun D, Poran A, Laughney AM, Wang Z, Sam J, Belenguer G, Farinas I, Elemento O et al. 2020. High-resolution mouse subventricular zone stem-cell niche transcriptome reveals features of lineage, anatomy, and aging. *Proc Natl Acad Sci U S A* **117**: 31448-31458.

Xu L, Nguyen JV, Lehar M, Menon A, Rha E, Arena J, Ryu J, Marsh-Armstrong N, Marmarou CR, Koliatsos VE. 2016. Repetitive mild traumatic brain injury with impact acceleration in the mouse: Multifocal axonopathy, neuroinflammation, and neurodegeneration in the visual system. *Exp Neurol* **275 Pt 3**: 436-449.

Xu X, Cowan M, Beraldo F, Schranz A, McCunn P, Geremia N, Brown Z, Patel M, Nygard KL, Khazaee R et al. 2021. Repetitive mild traumatic brain injury in mice triggers a slowly developing cascade of long-term and persistent behavioral deficits and pathological changes. *Acta Neuropathol Commun* **9**: 60.

Yi F, Pereira L, Hoffman JA, Shy BR, Yuen CM, Liu DR, Merrill BJ. 2011. Opposing effects of Tcf3 and Tcf1 control Wnt stimulation of embryonic stem cell self-renewal. *Nat Cell Biol* **13**: 762-770.

Zhao L, Han S, Su H, Li J, Zhi E, Li P, Yao C, Tian R, Chen H, Chen H et al. 2022. Single-cell transcriptome atlas of the human corpus cavernosum. *Nat Commun* **13**: 4302.

Zywitza V, Misios A, Bunatyan L, Willnow TE, Rajewsky N. 2018. Single-Cell Transcriptomics Characterizes Cell Types in the Subventricular Zone and Uncovers Molecular Defects Impairing Adult Neurogenesis. *Cell Rep* **25**: 2457-2469 e2458.

## Figure legends

**Fig.1. Major cell types in adult SVZ and cell type specific markers at Single-Cell Profiling.**

**A.** Workflow of sample preparation, single-nucleus RNA-seq and the downstream analysis.

**B.** Neurological Severity Score (NSS) of control group and mTBI group. 3 mice in each group were included. The *t*-test was used to determine statistical significance, **P≤0.01.

**C.** Bright-field image of the SVZ, the sampling area is circled by the dotted line.

**D.** Uniform manifold approximation and projection (UMAP) visualization of 15,265 cell from the SVZ of the control and the mTBI group, 17 cell clusters were detected.

**E.** Heat map showing differentially expressed genes in each cell type, dot plot showing the gene expression level in the indicated GO terms in each cell type.

**F.** Violin plots showing expression level of representative genes that were explicitly expressed in each cell population.

**Fig.2. Transcription characteristics and heterogeneity of each cell type in response to the mTBI.**

**A.** Bar plot showing the cell count proportion of 7 major cell types in the control and mTBI group.

**B.** Pie chart showing the proportion of cells in 16 clusters in the control and mTBI group.

**C.** Kyoto Encyclopedia of Genes and Genomes (KEGG) analysis of the major cell types.

**D.** GO analysis showing enriched terms in 7 major cell types (left: up-regulated, right: down-regulated in the mTBI).

**CE.** Enrichment of representative signaling pathways on UMAP plot.

**Fig.3. Alterations of the cell-cell crosstalk in the SVZ after mTBI.**

**A.** Cell-cell communication signaling network among major cell types analyzed with CellChat. The width of the lines indicates the number of pairs, different colours represent different signal sources.

**B.** Bar plot showing the number of inferred interactions and the proportion of interaction strength in the control and the mTBI.

**C.** The location of major cell types based on the count of their significant incoming (Y-axis) or outgoing (X-axis) signaling pattern.

**D.** Signal pathway network and bar plot showing the expression of specific signaling pathways in the control and the mTBI SVZ. Width of the lines indicates signal strength.

**E.** Dot plot showing the pairing of ligands (red)-receptors (blue) in the control and the mTBI SVZ.

**Fig.4. NSC & astrocyte diversities in the niche and their alteration post-mTBI.**

**A.** UMAP plot showing 5 sub-types of NSCs & astrocytes.

**B.** Dot plot showing the representative markers for each sub type. A gradient

of light purple to yellow indicates inhibition to activation of the term. Size of the bubble indicates the P-value.

**C.** Bar plot showing the proportion of each cell types in the control and mTBI group.

**D.** Upper: volcano plot showing DEGs in the control and mTBI group. Lower: violin plot showing up-regulated and down-regulated genes in each cell type. The *t*-test was used to determine statistical significance, ****P≤0.0001.

**E.** SCENIC results of the control and mTBI group. Major regulators were exhibited, their corresponding enriched DNA-binding motifs were shown in right column.

**F.** Ridge plot showing the expression of *Tcf7l1*.

**G.** Protein-protein interaction (PPI) networks of TFs and miRNAs in neuroblast (upper), and astrocyte, qNSC, early aNSC (lower).

**Fig.5. Pseudotime analysis revealed reprogramming trajectory of NSCs after injury**.

**A.** Upper: coloured cells plotted onto the UMAP according to the pseudotime. Lower: monocle2-generated pseudo-temporal trajectory of NSC & astrocyte.

**B.** Different astrocyte & NSC sub-types along the pseudotime trajectory.

**C.** Cell ordering from different differentiation stages along the pseudotime trajectory.

**D.** Bar plot showing the proportion of each differentiation stage in the control and the mTBI.

974 **E.** Left: heatmap showing gene expression patterns along the pseudotime
975 (1,000 genes). Right: 3 clusters were identified based on the expression
976 dynamics, GO term for each cluster was displayed on the right column.
977 **F.** Expression pattern of representative genes during differentiation from
978 aNSC to neuroblasts. States are shown in colours, and branches are indicated
979 by lines.

980 **Fig.6. Knockdown of Tcf7l1 induced differentiation of NE-4C cells**
981 **towards neuron lineage cells *in vitro*.**

982 **A.** Schematic showing the siRNA knockdown approach on NE-4C cell line.
983 **B.** Cy3 signal indicating successful transfection of cells using siRNA.
984 **C.** qPCR results of *Tcf7l1* in each group. Expression levels were normalized to
985 *Gapdh,* 3 technical duplicates were performed in individual qPCR
986 experiments. The *t*-test was used to determine statistical significance, *P≤0.05,
987 **P≤0.01, ***P≤0.001, ****P≤0.0001, ns. denotes for not significant.
988 **D.** qPCR assay of marker genes of different NSCs, progenitors and neuroblasts
989 under different treatment. Expression levels were normalized to *Gapdh,* 3
990 technical duplicates were performed in individual qPCR experiments. The *t*-
991 test was used to determine statistical significance, *P≤0.05, **P≤0.01,
992 ***P≤0.001, ****P≤0.0001, ns. denotes for not significant.
993 **E, F.** Immunofluorescence staining against THBS4 (CE) and DCX (F) in
994 cultured cells under different treatments. Sections are counterstained with
995 DAPI.

**Fig.7. Suppressing *Tcf7l1* promoted neuronal differentiation of the SVZ NSCs after mTBI.**

**A.** Upper: Schematic diagram of in vivo experiment. Lower: Schematic representing the adenovirus injection, along with its genetic sequence.

**B.** GFP signal indicating successful SVZ injection of the adenovirus.

**C.** qPCR assay of *Tcf7l1* indicating successful knockdown of *Tcf7l1* in the SVZ. Expression levels were normalized to *Gapdh*. 3 technical duplicates were performed in individual qPCR experiments.

**D, E.** Immunofluorescence staining (CD) and $THBS4^{+}MKI67^{+}/THBS4^{+}$ cell counting results (E) for THBS4 and MKI67 in the SVZ region from sham, mTBI+control vector, and mTBI+*Tcf7l1* vector. Tissues are counterstained with DAPI. The *t*-test was used to determine statistical significance, *P≤0.05.

**F, G.** Immunofluorescence staining (F) and $DCX^{+}BrdU^{+}/BrdU^{+}$ cell counting results (G) for DCX and BrdU in the SVZ region from sham, mTBI+control vector, and mTBI+*Tcf7l1* vector. Tissues are counter-stained with DAPI. The *t*-test was used to determine statistical significance, **P≤0.01.

**Figure 1**



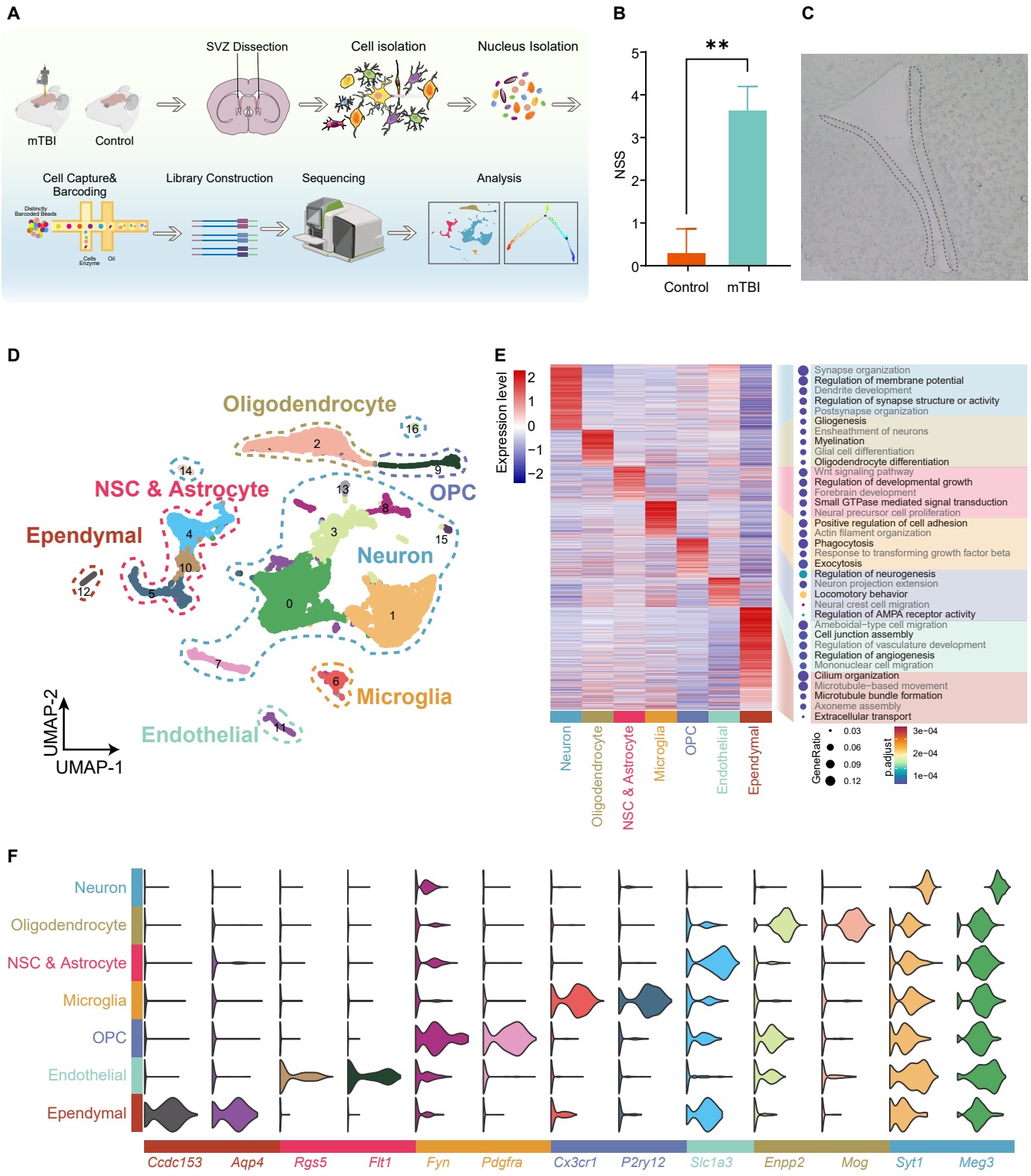

# Figure 2



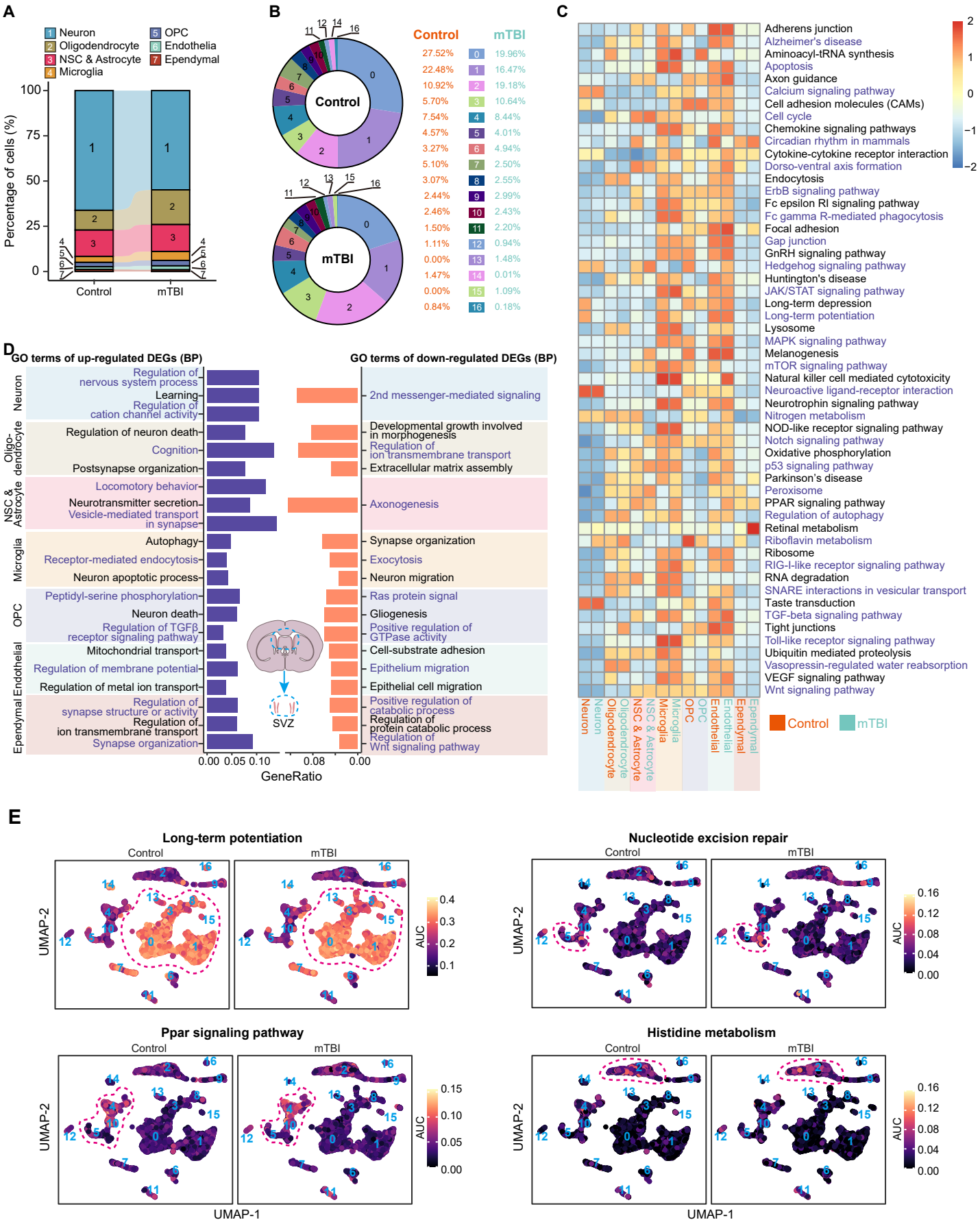

Figure 3



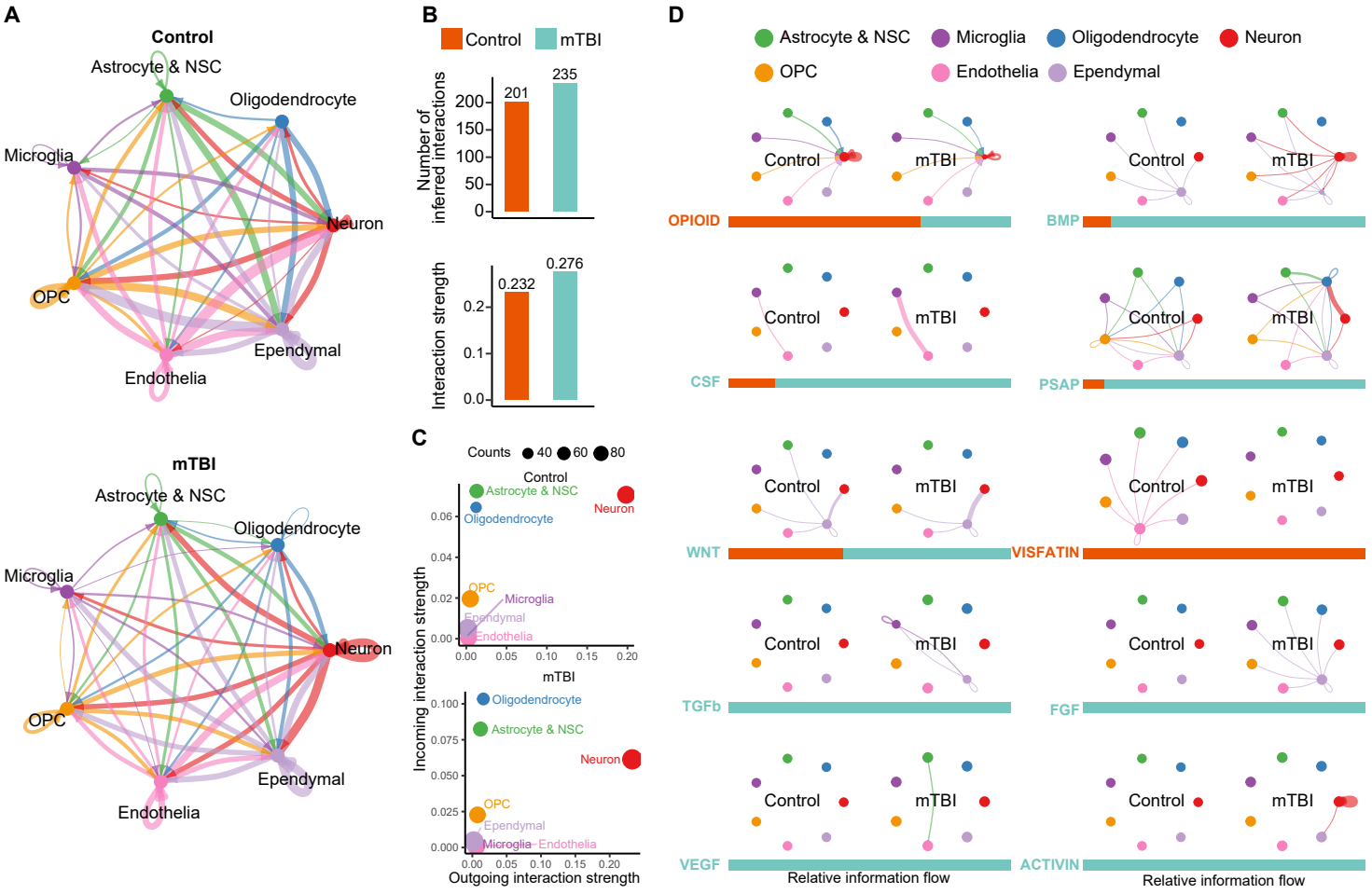


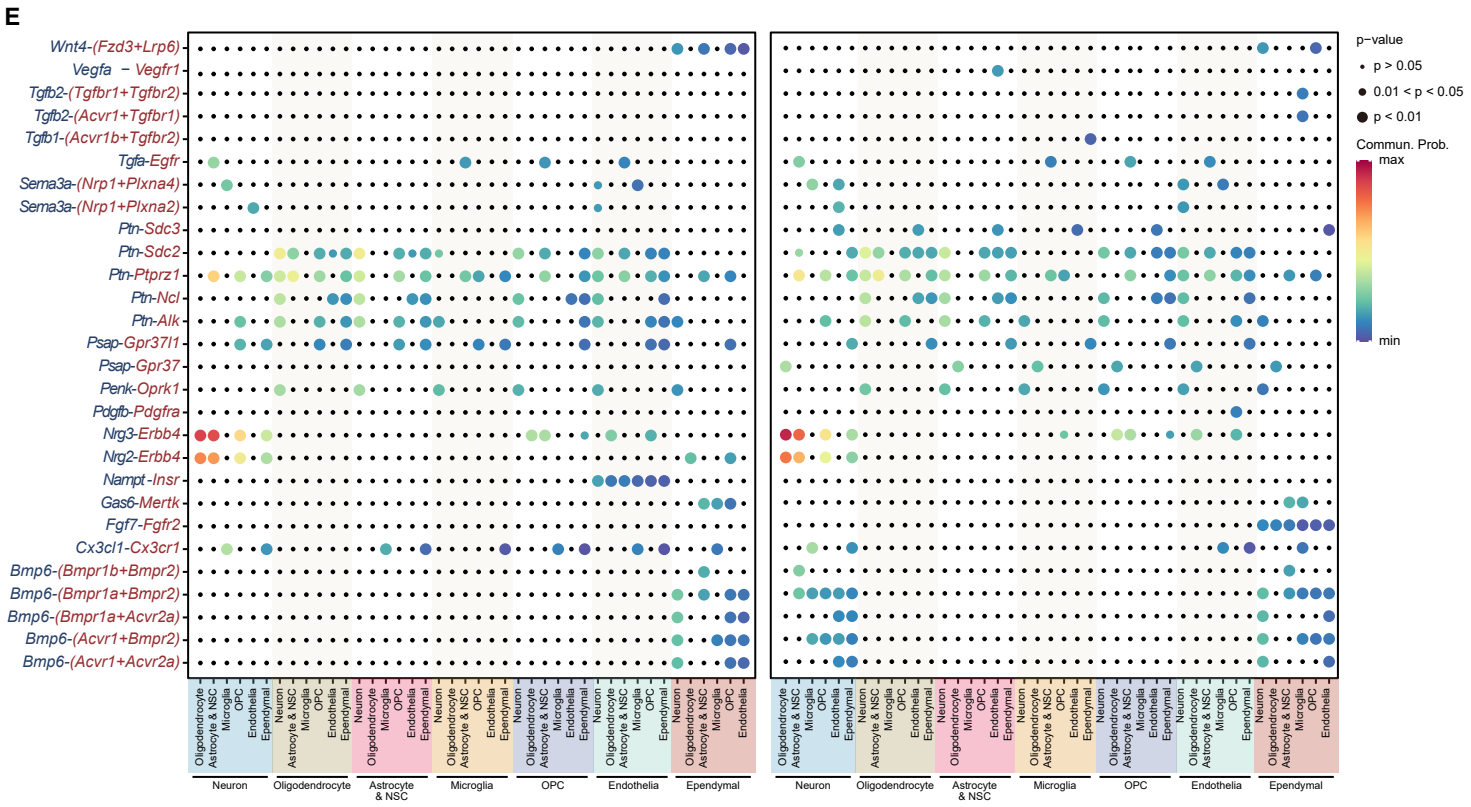

# Figure 4



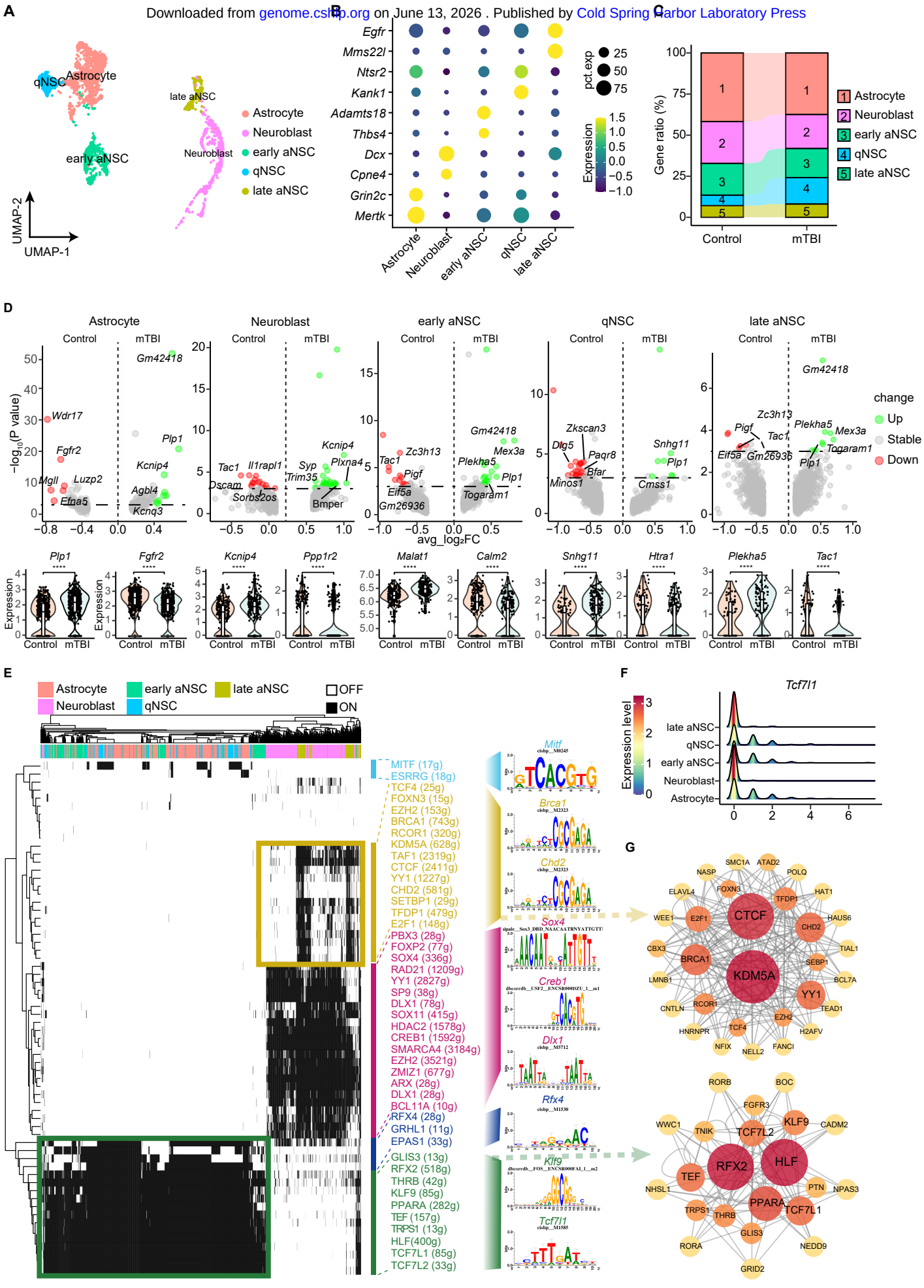

**Figure 5**



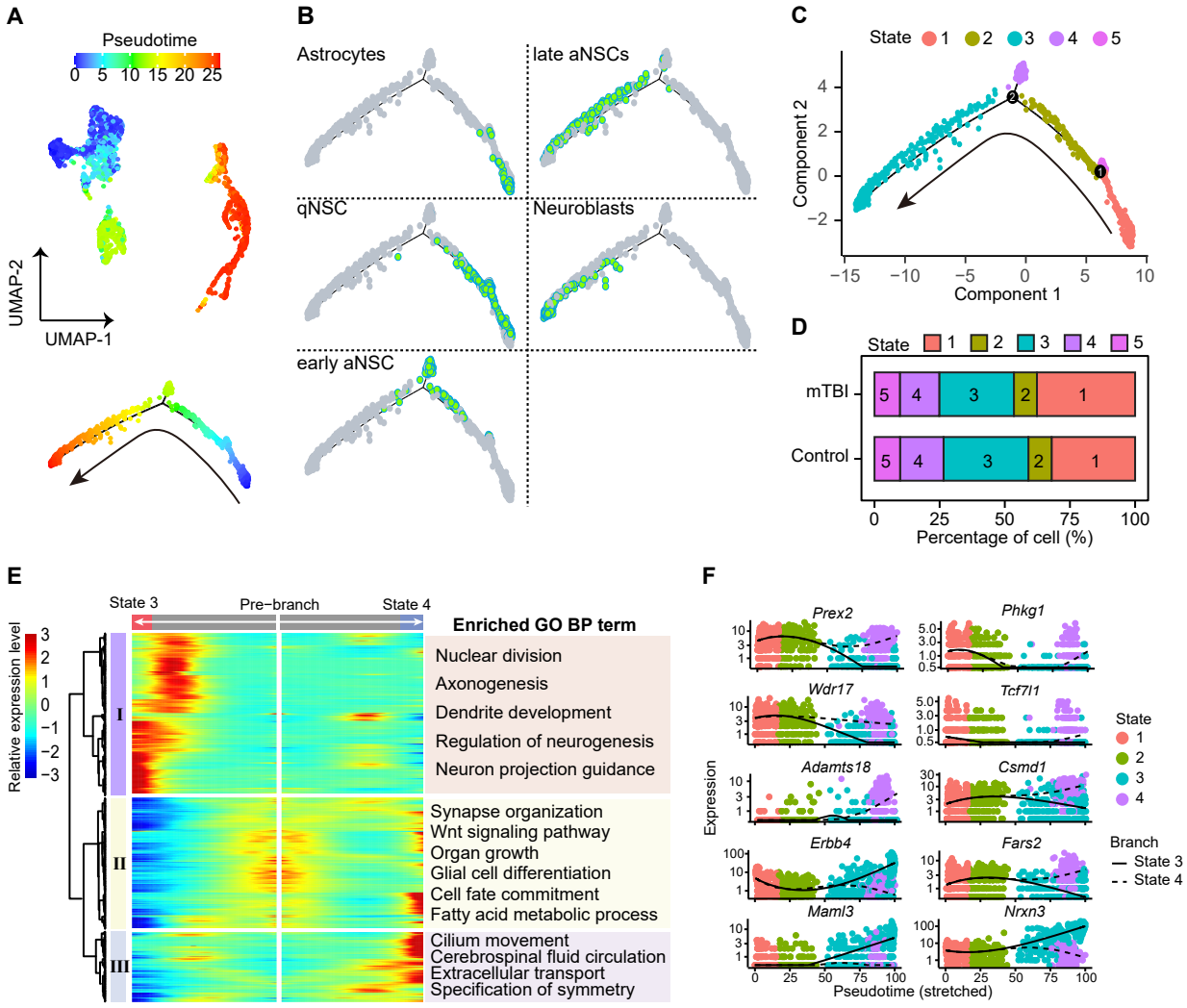

# Figure 6



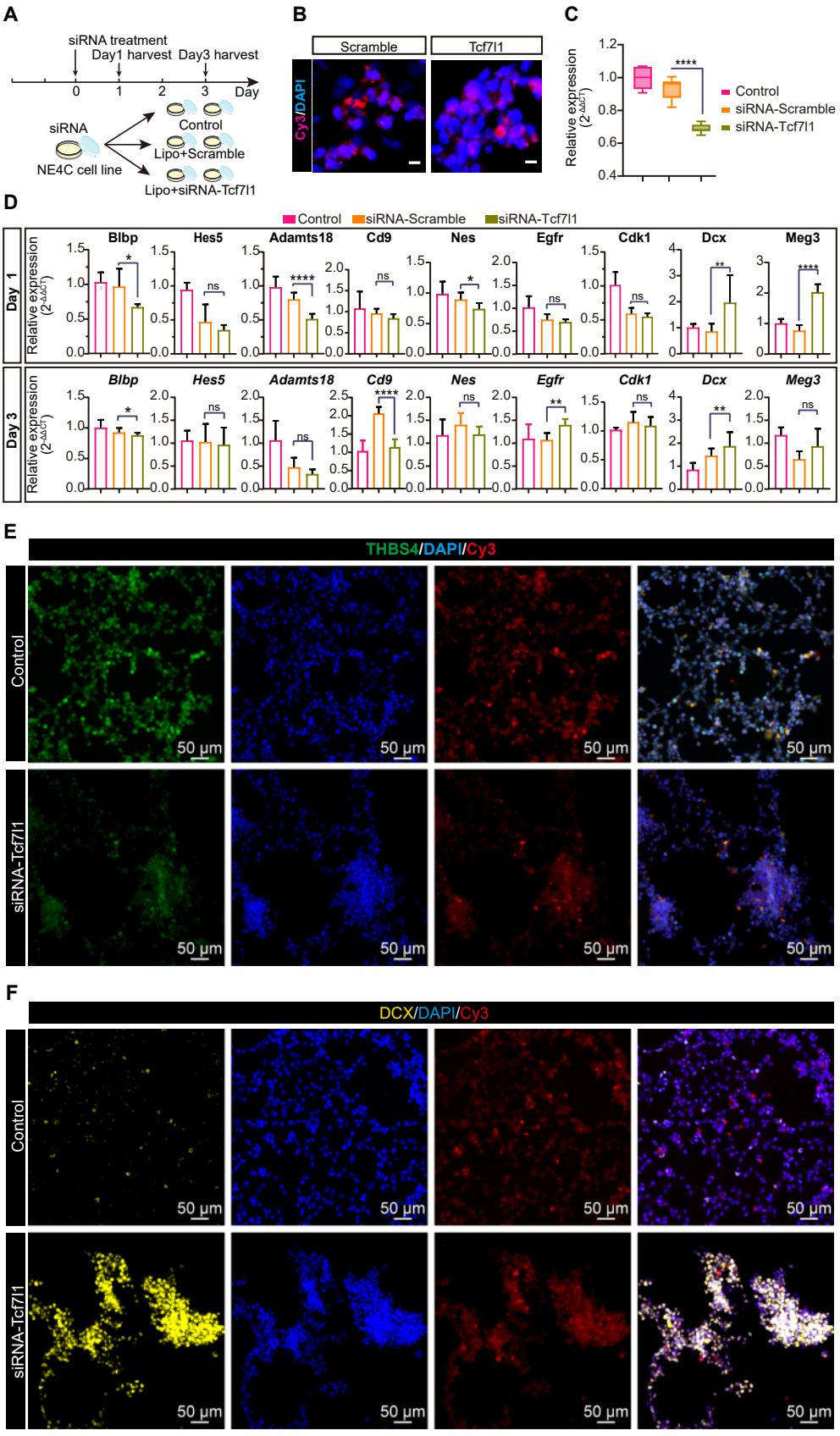

**Figure 7**